J Mater Sci (2026) 61:19522–19536

Composites & nanocomposites

Construction of Au nanocup@Cu_2O nanocomposites for plasmon-mediated photocatalysis of methyl orange

Xi-Hao Zhang[1], Jie Liu[1,*], Lan Chen[1], Zhigang Zhou[1], and Tian-Song Deng[1,*]

[1] *School of Electronics and Information Engineering, Hangzhou Dianzi University, Hangzhou 310018, People's Republic of China*

Received: 11 March 2026
Accepted: 17 May 2026

ABSTRACT

Combining gold nanostructures with cuprous oxide semiconductors can integrate the plasmon resonance effects of noble metals with the visible-light-responsive properties of semiconductors, offering a novel approach to enhancing photocatalytic performance. In this study, we employed Au nanocup as the core component—a nanomaterial featuring a three-dimensional asymmetric structure that exhibits remarkable localized surface plasmon resonance and high specific surface area. By varying the amount of copper precursor, we successfully synthesized a series of Au nanocup@Cu_2O core–shell composites with different Cu_2O shell thicknesses. The influence of shell thickness on the optical properties and photocatalytic performance was systematically investigated. In the photocatalytic degradation of methyl orange under visible-light irradiation, the optimized composite demonstrated significantly enhanced activity, with the degradation efficiency being more than 12 times higher than that of pure Au nanocup or pure Cu_2O. The performance improvement is attributed to two main factors: the efficient transfer of plasmon resonance energy from the Au nanocup to the Cu_2O shell, which promotes charge generation and separation, and the formation of a heterojunction interface that facilitates charge transport. This study provides new insights for designing efficient photocatalysts and shows promising potential for environmental remediation applications.

Introduction

With rapid industrialization, water pollution caused by organic contaminants—particularly toxic and persistent dye effluents—has become a critical issue threatening ecological safety and public health [1, 2]. Conventional treatment methods such as adsorption and flocculation are often insufficient for complete pollutant degradation. In contrast, photocatalytic technology has attracted widespread attention due to its ability to utilize solar energy directly to decompose pollutants into harmless substances [3, 4]. Among various photocatalysts, cuprous oxide (Cu_2O), a typical p-type semiconductor, exhibits promising potential

---

Handling Editor: Oleksandr Savatieiev.

Address correspondence to E-mail: liujie4209@hdu.edu.cn; dengts@pku.edu.cn

Springer https://doi.org/10.1007/s10853-026-13004-3

owing to its suitable bandgap (~ 2.17 eV), good visible-light response, and strong valence-band oxidation capability [5, 6]. However, pure Cu_2O suffers from drawbacks such as high recombination rates of photogenerated charge carriers, limited light absorption range, and photocorrosion, which hinder its practical application [7].

In recent years, noble metal–semiconductor heterojunctions have emerged as an important strategy for improving photocatalytic efficiency by synergistically integrating plasmonic resonance effects with semiconductor band engineering [8]. Gold (Au) nanostructures are particularly attractive due to their tunable localized surface plasmon resonance (LSPR) properties and their role as electron-transfer mediators that promote interfacial charge separation [9, 10]. The combination of Au with p-type semiconductors such as Cu_2O can form effective Schottky junctions, facilitating directional separation of photogenerated carriers [11, 12].

However, conventional spherical or rod-like Au nanomaterials often exhibit narrow light absorption ranges, insufficient catalytic active sites, and difficulty in forming uniform and intimate heterojunction interfaces due to their high structural symmetry and limited specific surface area [13, 14]. To overcome these limitations, researchers have focused on developing novel plasmonic nanostructures. For instance, Au@Cu_2O core–shell nanoparticles have been shown to enhance charge separation effectively [15], while Janus and core–satellite nanostructures further optimize charge transport pathways by constructing multiple interfaces [16, 17]. Recently, Au nanocups with three-dimensional asymmetric structures have gained considerable attention owing to their unique open-hollow configuration, tunable multi-mode LSPR, and high specific surface area [18]. Their abundant surface curvature and "hot-spot" distribution not only increase catalytic site density but also provide an ideal substrate for uniform epitaxial growth of semiconductor materials [19, 20]. Studies have demonstrated that coupling Au nanocups with semiconductors can significantly enhance the local electromagnetic field and improve photocatalytic performance [21, 22].

Despite considerable progress in Au-Cu_2O composite photocatalysts, a key challenge remains in precisely controlling the heterojunction interface structure—such as the semiconductor shell thickness—to maximize the plasmonic–semiconductor synergy [23, 24]. Shell thickness directly affects light absorption, charge transfer efficiency, and carrier lifetime, thereby determining the ultimate photocatalytic activity [25, 26]. Moreover, the energy transfer mechanisms between asymmetric plasmonic structures and semiconductors, particularly hot-electron injection and the role of interfacial built-in electric fields, require further elucidation [27].

Recent studies have provided profound insights into photocatalytic mechanisms and material design. For example, Cao et al. reported enhanced reactive oxygen species generation via a built-in electric field (BIEF) in Au-Cu_2O nanodumbbells, enabling efficient near-infrared photocatalytic therapy, which offers a new perspective on the critical role of interfacial electric fields in driving charge separation [28]. Yang et al. significantly enhanced plasmonic photocatalytic performance by tuning modal coupling in Au@Cu_2O@Au core–shell-satellite nanostructures, highlighting the importance of optical mode regulation in complex nanoarchitectures [29]. Zhang et al. achieved enantioselective photocatalysis using chiral Au@Cu_2O-Cu_2S nanoparticles, demonstrating the great potential of interface engineering in controlling reaction selectivity [30]. Furthermore, comprehensive reviews by Sayed et al. on non-noble plasmonic metal-based photocatalysts [31] and by Zhou et al. on the synthesis and applications of noble-metal alloy and intermetallic nanocrystals [32] have provided important theoretical foundations and material libraries for the rational design of novel composite catalysts.

Particularly noteworthy are recent advances in the quantitative study of interfacial charge dynamics in Au-Cu_2O systems. Ahn et al. quantitatively analyzed the electronic transfer contribution of Au to semiconductor photocatalysts through combinatorial synthesis and single-particle excitation experiments, providing a powerful tool for understanding plasmonic enhancement mechanisms at the single-particle level [33]. Wu et al. revealed the strong dependence of interfacial charge transfer on different crystal facets in Cu_2O-ZnO heterostructures, emphasizing the importance of controlling interfacial atomic structures [34].

In terms of application expansion, Au-Cu_2O composites have demonstrated remarkable versatility. For instance, the Au-Pt/Cu_2O/ReS_2 system constructed by Huang et al. achieved high efficiency and controllable product selectivity in CO_2 photoreduction [35]. The Au@Cu_2O-Ta_3N_5 core–shell spheres developed by Zhu et al. significantly enhanced photocatalytic hydrogen evolution performance [36]. In environmental sensing, the Au/Cu_2O/ZnO SERS

Scheme 1 Schematic diagram of the synthetic process.

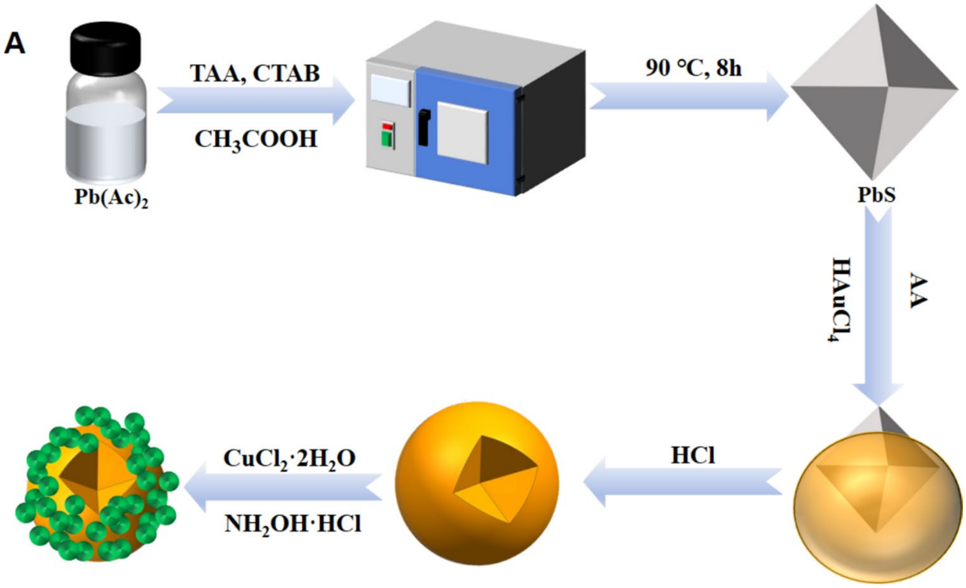

substrate prepared by Li et al. enabled ultrasensitive detection of pesticide residues [37]. These advances indicate that through sophisticated interface and structural engineering, Au-Cu_2O composites hold broad application prospects in multiple key fields, including environmental remediation, clean energy, and intelligent sensing. However, integrating Au nanocups with their unique optical properties with Cu_2O semiconductors and systematically investigating their shell-thickness-dependent photocatalytic performance and mechanisms remain a research direction that warrants in-depth exploration.

In light of the aforementioned challenges and recent advances, this study designs and constructs Au nanocup@Cu_2O heterojunction nanocomposites. Different from conventional spherical or rod-like gold nanostructures, we employ Au nanocups with a three-dimensional asymmetric open-hollow configuration as the core. Compared with traditional Au nanospheres or nanorods, this unique geometry provides a higher specific surface area, richer distribution of local electromagnetic field “hot spots”, and more accessible heterojunction interfaces. Through a low-temperature surfactant-assisted strategy, we achieve precise control over the Cu_2O shell thickness, ranging from sparse nanoparticle coverage to a dense continuous layer, and establish a quantitative correlation among shell thickness, LSPR evolution, and photocatalytic performance. Furthermore, by combining systematic experiments with finite-difference time-domain (FDTD) simulations, we reveal how the Au nanocup@Cu_2O structure achieves local electric field enhancement and how the Cu_2O shell modulates the dielectric environment and charge separation dynamics. The influence of Cu_2O shell thickness on the photocatalytic degradation of MO is systematically investigated. Remarkably, compared with pure Au nanocups or pure Cu_2O, the optimized Au nanocup@Cu_2O composite exhibits a more than 12-fold enhancement in degradation efficiency, demonstrating the strong synergistic effect between the plasmonic Au nanocup and the Cu_2O semiconductor. This work not only deepens the understanding of the structure–performance relationship in plasmon–semiconductor heterojunctions but also provides a new design paradigm for high-performance photocatalysts with potential applications in rapid environmental remediation.

Results and discussion

Scheme 1 illustrates the fabrication process of the Au nanocup@Cu_2O core–shell nanostructures. The specific synthesis procedure is as follows: First, PbS nano-octahedra were synthesized as templates using $Pb(Ac)_2$ as the precursor in a CH_3COOH medium containing the surfactant CTAB and the sulfur source TAA, with reaction at 90 °C for 8 h. Its extinction spectrum and SEM images are shown in Figure S1.

The PbS nanocrystals exhibited uniform size distribution with edge lengths of approximately 50 nm and well-defined morphology, providing an ideal template foundation for subsequent Au nanocup synthesis. Subsequently, using PbS nanocrystals as cores, gold was grown on their surfaces by adding $HAuCl_4$ and ascorbic acid (AA) to form PbS@Au structures. Its extinction spectrum and SEM images are shown in Figure S2. During this process, CTAB acted as a morphology-directing agent, promoting uniform Au deposition. Next, the PbS template was selectively etched away by adding hydrochloric acid, yielding hollow Au nanocup structures. Finally, under low-temperature conditions [38], Au nanocups slowly deposit Cu^{2+} and oxidize in a surfactant environment containing SDS, forming Cu_2O shell, eventually creating Au nanocup@Cu_2O composite structure.

Figure 1 presents the optical properties, morphological features, and elemental composition analysis of the Au nanocups and the corresponding Au nanocup@Cu_2O core–shell structures. Figure 1A shows the UV–Vis absorption spectra of Au nanocups and Au nanocup@Cu_2O. The Au nanocups exhibit a distinct LSPR absorption peak around 570 nm, which is closely related to their unique hollow cup-like structure and size. Upon formation of the Au nanocup@Cu_2O composite, the spectrum changes significantly: the LSPR peak becomes less pronounced and redshifts, while an absorption band emerges around 500 nm, attributed to the band-edge absorption of Cu_2O. This indicates effective electronic coupling and interfacial interaction between the Au nanocups and the Cu_2O shell. Figures 1B and C show scanning electron microscopy (SEM) images of Au nanocups and Au nanocup@Cu_2O, respectively. The SEM images reveal that the Au nanocups possess a regular hollow-open structure with relatively smooth surfaces and a lateral diameter of approximately 70 nm. After Cu_2O coating, the surface becomes noticeably rougher. Due to the low-temperature conditions that slow down the Cu_2O deposition rate, a uniform layer of Cu_2O particles is observed attached to the Au nanocups. Energy-dispersive X-ray spectroscopy (EDS) elemental mapping analysis (Figs. 1D–G) further confirms the presence of Au, Cu, and O. The Au signal is concentrated in the interior region of the cup, while Cu and O signals are distributed across the entire surface, corroborating the uniform coating and structural integrity of the Cu_2O shell.

To further confirm the core–shell structure and directly visualize the Cu_2O shell thickness, TEM imaging was performed on the representative Au@

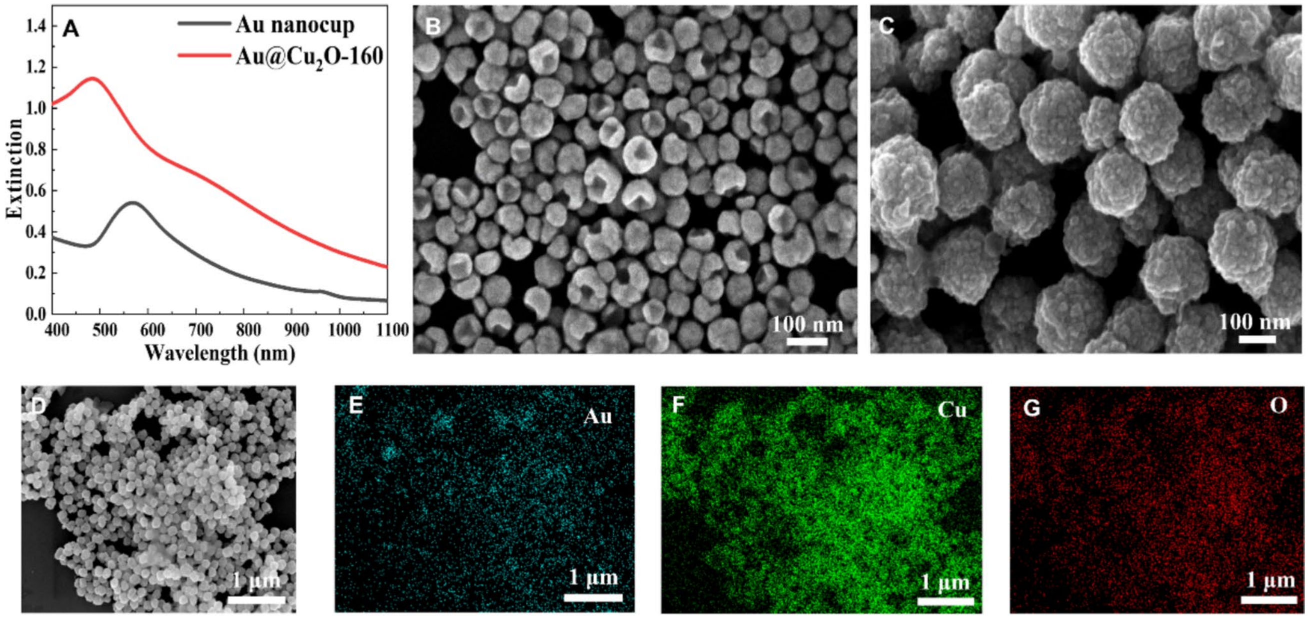

Figure 1 Characterization of Au nanocup and Au nanocup@Cu_2O structures. **A** Spectroscopic analysis and photocatalytic performance of the Au nanocup@Cu_2O exhibiting optimal activity. **B** SEM image of the Au nanocup. **C** SEM image of the Au nanocup@Cu_2O with the highest photocatalytic efficiency. **D** EDS spectrum of the Au nanocup@Cu_2O demonstrating elemental composition of the photocatalytically active sample.

Cu_2O-160 composite. As shown in Figure S3, the TEM images clearly reveal the distinct core–shell architecture of the Au@Cu_2O-160 nanostructure. The Au nanocup core appears as a dark-contrast open-hollow cup-like structure, while the Cu_2O shell exhibits a gray-contrast uniform layer surrounding the Au core. The inset schematic model in Figure S3A further illustrates the spatial configuration of the Au nanocup core and the Cu_2O shell. These TEM observations provide direct and unambiguous evidence for the successful synthesis of well-defined Au@Cu_2O core–shell nanostructures with a uniform and continuous Cu_2O coating.

Figure 2 illustrates the morphological evolution with varying Cu_2O shell thicknesses and its impact on the optical properties of the Au nanocup@Cu_2O composites. Figure 2A presents the normalized UV–Vis extinction spectra of the composites with different shell thicknesses. As the shell thickness increases, the LSPR peak of the Au nanocups located around 600 nm gradually redshifts and diminishes in intensity, indicating the growth of Cu_2O on the Au nanocup surface and the progressive increase in shell thickness. Concurrently, the band-edge absorption peak of Cu_2O in the 400–500 nm range intensifies. The spectral data suggest that shell thickness not only affects the LSPR resonance position but also modulates the coupling strength between the Au nanocup and the Cu_2O semiconductor. Figure 2B quantitatively summarizes the relationship between the overall particle size and Peak 1 position of the Au nanocup@Cu_2O composites as a function of the added Cu precursor volume. As the volume of copper precursor increases, the overall size of the composites grows from approximately 83 nm to 176 nm. Peak 1 redshifts from 435 to 485 nm, a shift of about 50 nm, primarily attributed to changes in the dielectric environment and enhanced plasmonic coupling. SEM images in Fig. 2C–F visually demonstrate the morphological evolution with increasing shell thickness. From (C) to (F), the Cu_2O shell transitions from a thin, sparse particle coverage to a rough, densely packed layer, indicating favorable epitaxial growth of Cu_2O on the Au nanocup surface. The shell thickening process proceeds without significant aggregation or structural collapse, confirming the good thickness controllability and structural stability of the synthesis method.

To quantitatively establish the relationship between Cu_2O shell thickness and photocatalytic performance, the shell thickness was estimated based on the SEM measurement results in Fig. 2B.The average diameter of the bare Au nanocup core was measured to be

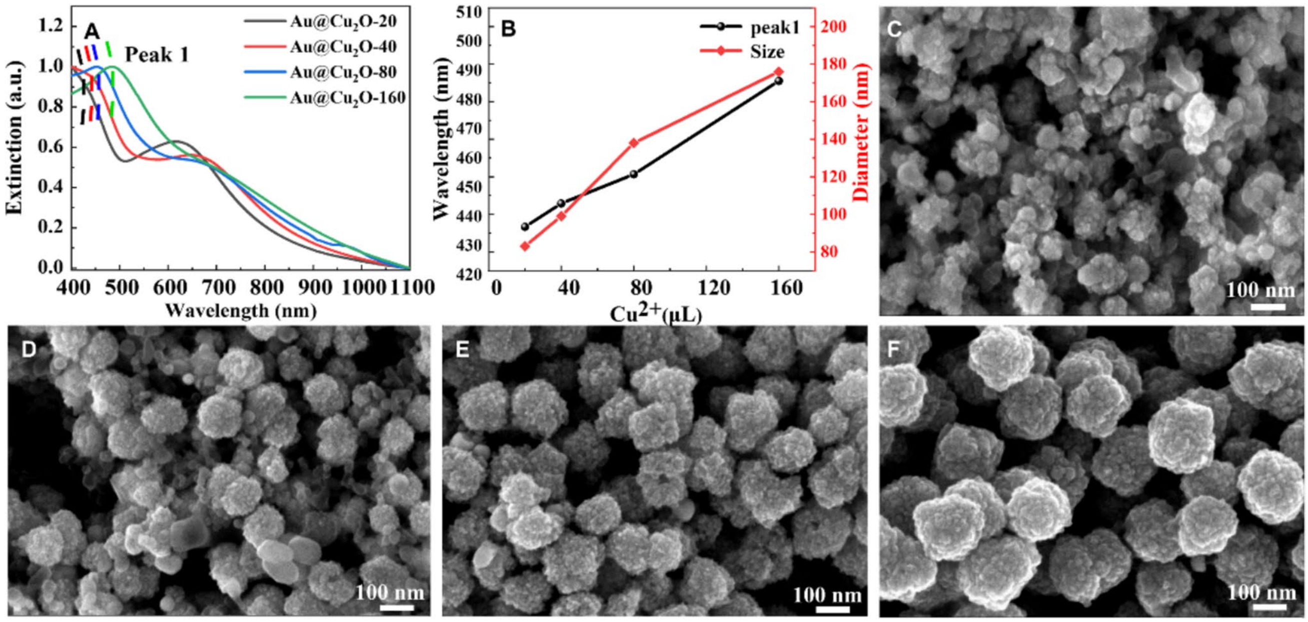

Figure 2 Au nanocup@Cu_2O nanocomposite samples with varying amounts of Cu_2O particles. **A** Extinction spectra of Au nanocup@Cu_2O with different Cu_2O particle quantities. **B** Variations in Peak 1 position and size for Au nanocup@Cu_2O samples. SEM images of **C** Au@Cu_2O-20; **D** Au@Cu_2O-40; **E** Au@Cu_2O-80; **F** Au@Cu_2O-160, illustrating the coverage of Au nanocup@Cu_2O obtained by adding varying volumes of $CuCl_2·2H_2O$, resulting in different Cu_2O particle loadings.

approximately 70 nm (Fig. 1B).Since the size of the Au core remains unchanged after the Cu_2O shell layer is coated, the thickness of the Cu_2O shell layer can be approximately calculated by subtracting the diameter of the Au nanocup core from the total particle size of the composite material. As the volume of the Cu precursor increased from 20 to 160 μL, the overall particle size of the composite material rose from approximately 83 nm to 176 nm. The Cu_2O shell thicknesses corresponding to Au@Cu_2O-20, Au@Cu_2O-40, Au@Cu_2O-80 and Au@Cu_2O-160 are approximately 13 nm, 35 nm, 68 nm and 106 nm, respectively. These estimated thickness values are consistent with the gradual redshift of the LSPR peak observed in Fig. 2B (from 435 to 485 nm) and the monotonically increasing trend of the degradation rate constant shown in Fig. 4E, confirming that a thicker Cu_2O shell is conducive to enhancing light absorption and promoting charge separation, thereby improving the photocatalytic efficiency.

Figure 3 presents the X-ray photoelectron spectroscopy (XPS) results for the representative and most photocatalytically efficient Au nanocup@Cu_2O composite, providing further insight into its surface chemical states and elemental composition. In the high-resolution Au 4*f* spectrum (Fig. 3A), the binding energies of Au $4f_{7/2}$and Au $4f_{5/2}$ are located at approximately 84.48 eV and 88.18 eV, respectively, corresponding to metallic gold (Au^0). No significant binding energy shift or oxidized state signals are observed, indicating that the Au nanocups retain their metallic character during the composite formation. The high-resolution Cu 2*p* spectrum (Fig. 3B) displays a pair of peaks at about 932.5 eV and 952.4 eV, assigned to Cu $2p_{3/2}$ and Cu $2p_{1/2}$, respectively, with no apparent satellite peaks. These binding energy positions are highly consistent with the characteristics of Cu^+ (i.e., cuprous oxide), confirming that copper predominantly exists in the Cu^+ oxidation state and that the peak shapes and narrow full-width at half-maximum suggest good crystallinity and chemical purity of the Cu_2O shell. The high-resolution O 1*s* spectrum (Fig. 3C) shows a main peak at approximately 530.8 eV, attributed to lattice oxygen (O^{2-}) in Cu_2O, further verifying the formation of the Cu_2O phase. The XPS analysis systematically confirms that in the Au nanocup@Cu_2O composite, gold is in the metallic state, copper is in the Cu^+ oxidation state, and oxygen primarily exists as lattice oxygen, thereby clarifying its chemical composition and surface state and providing key information for understanding its interfacial

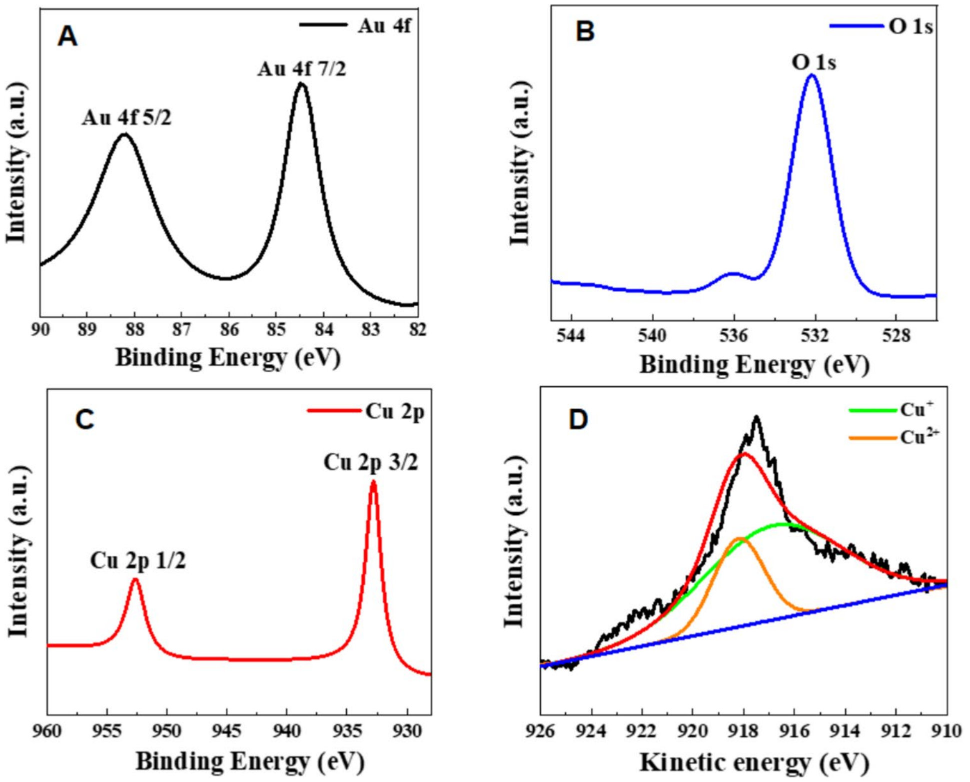

Figure 3 XPS spectrum of Au@Cu_2O-160. **A** XPS spectrum illustrating the Au 4*f* core-level peaks. **B** Spectrum showing the Cu 2*p* core-level peaks. **C** Spectrum depicting the O 1*s* core-level peaks. **D** Cu LMM Auger spectrum.

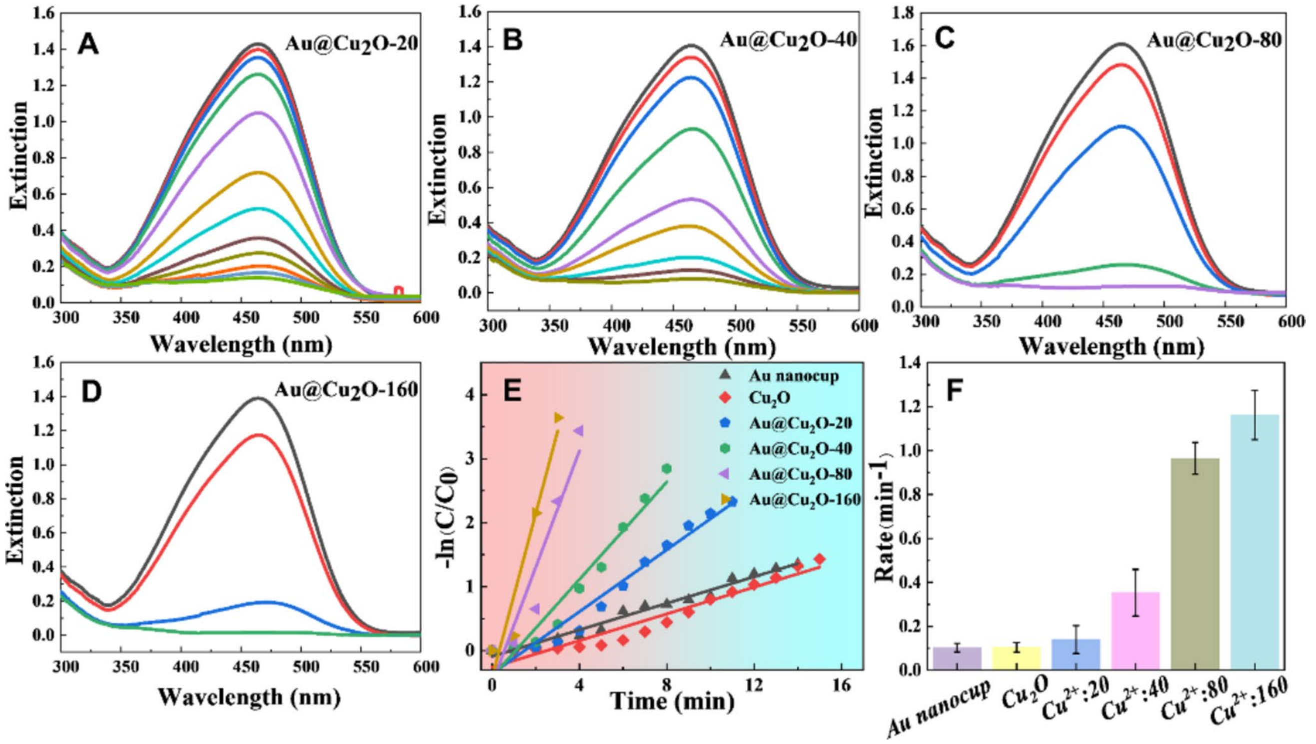

Figure 4 Time-dependent UV–Vis absorption spectra of methyl orange (MO) reduction catalyzed by different nanoparticles with $NaBH_4$: **A** Au@Cu_2O-20; **B** Au@Cu_2O-40; **C** Au@Cu_2O-80; **D** Au@Cu_2O-160. **E** Kinetic linear fit curves for MO reduction using various catalysts (Au nanocups; Au@Cu_2O nanoparticles with four different copper ion concentrations; Cu_2O). **F** Conversion rates of MO reduction catalyzed by the different catalysts.

properties. In order to further confirm the valence state of copper in the Au@Cu_2O-160 composite material, Cu LMM auger electron spectroscopy analysis was conducted. As shown in Fig. 3D, the Auger spectrum fitting is decomposed into two distinct peaks. The main peak at approximately 916.8 eV (kinetic energy) is the characteristic peak of Cu^+ in Cu_2O, while the secondary peak at approximately 918 eV corresponds to Cu^{2+}. The fitting results show that Cu^+ is the main oxidation state, and the peak intensity of Cu^+ is higher than that of Cu^{2+}. The presence of a small amount of Cu^{2+} can be attributed to the surface oxidation of the Cu_2O shell when exposed to air [39]. This idea is consistent with the Cu 2*p* spectrum (Fig. 3C), in which no obvious satellite peaks (typically located at 940–945 eV) were observed, further confirming that Cu^{2+} is not a bulk component but only exists in the topmost layer. Therefore, the Auger analysis of Cu LMM clearly demonstrated that copper mainly exists in the Cu_2O shell in the form of Cu^+, which is crucial for maintaining the semiconductor properties and photocatalytic activity of the composite material.

X-ray diffraction (XRD) tests were conducted to verify the crystallinity and phase purity of Au@Cu_2O-160 composites. As shown in Figure S4, the XRD patterns reveal clear diffraction peaks corresponding to the metal Au and the cubic phase Cu_2O. The diffraction peaks located at 38.2°, 44.4°, 64.6° and 77.5° respectively belong to the (111), (200), (220) and (311) crystal planes of metallic Au, confirming the existence of the core of the crystalline Au nanocup. The diffraction peaks at 36.4°, 42.3°, 61.3° and 73.5° respectively belong to the (111), (200), (220) and (311) crystal planes of the cubic phase Cu_2O, confirming the successful formation of the crystalline Cu_2O shell. The sharp and intense diffraction peaks also indicate that both the Au core and the Cu_2O shell have good crystallinity, which is crucial for efficient charge transfer and photocatalytic performance.

Figure 4 systematically evaluates the photocatalytic performance of the Au nanocup@Cu_2O composites in degrading methyl orange under visible-light irradiation, with comparative analysis against the single-component Au nanocups and pure Cu_2O. Figures 4A–D show the time-dependent UV–Vis absorption spectra of MO solution under visible light when catalyzed by different Au@Cu_2O composites. As revealed by the UV–Vis absorption spectra, the characteristic absorption peak of MO at 462 nm, corresponding to the N=N chromophore, decreased rapidly under visible-light irradiation. In contrast, the absorption peak at approximately 300 nm, attributed to the benzene ring structure of MO, decreased at a much slower rate. The significant difference in the decay rates between the azo-bond-related peak and the benzene-ring-related peak indicates that the cleavage of the N=N double bond is the primary and preferential reaction step during the photocatalytic degradation process, while the subsequent mineralization of the benzene rings occurs at a slower rate. These spectral observations provide strong spectroscopic evidence that the photocatalytic degradation of MO by the Au nanocup@Cu_2O composite proceeds via the reductive cleavage of the central azo bond, leading to the formation of aniline-based intermediates [40]. It can be observed that as the Cu_2O shell thickness increases, the Au@Cu_2O composites exhibit progressively enhanced degradation efficiency. When Au@Cu_2O-160 is used as the catalyst, the characteristic absorption peak of MO (around 462 nm) decreases most significantly within the same time period, indicating its superior photocatalytic degradation capability. The photocatalytic activities of the individual components, namely pure Au nanocups and pure Cu_2O nanoparticles, were also evaluated under the same conditions. As shown in Figure S5, both single-component catalysts exhibit limited degradation efficiency. The characteristic absorption peak of MO at 462 nm decreases slowly over time for both catalysts, indicating insufficient photocatalytic activity of the individual components. This observation highlights the necessity of constructing the Au-Cu_2O heterojunction to achieve enhanced photocatalytic performance. Figure 4E compares the reaction rate constants (k) of different catalysts through kinetic fitting using a pseudo-first-order model. The linear fitting results show that the k values for all Au nanocup@Cu_2O composites are higher than those for the single-component Au nanocups and pure Cu_2O. The fastest composite exhibits a rate constant approximately 12.30 times that of pure Cu_2O and 12.45 times that of Au nanocups. This result demonstrates that the synergistic effect of the composite significantly enhances charge carrier separation efficiency and photocatalytic activity. Figure 4F presents a bar chart comparison of the degradation rates for different catalysts, providing a more visual representation of the photocatalytic rate enhancement achieved by the Au nanocup@Cu_2O composites. This rate difference is attributed to the plasmonic effect of the Au nanocups enhancing visible-light absorption, while the heterojunction formed with Cu_2O effectively promotes the separation and migration of photogenerated electron-hole pairs, thereby substantially improving the catalytic efficiency.

To confirm that the observed degradation of MO is indeed driven by photocatalysis rather than by chemical reduction from $NaBH_4$ alone, control experiments were performed under identical conditions. As shown in Fig. S6, the dark reaction (without light irradiation, Fig. S6A) showed a very low degradation rate, confirming that light irradiation is essential for the catalytic activity. Similarly, direct photolysis (without catalyst, Fig. S6B) resulted in negligible MO degradation, indicating that the presence of the Au@Cu_2O-160 catalyst is necessary for achieving efficient degradation. In sharp contrast, the complete photocatalytic system (with both light irradiation and the Au@Cu_2O-160 catalyst) achieved over 95% degradation within 3 min. These control experiments clearly demonstrate that the efficient degradation of MO arises from the synergistic effect of visible light excitation and the Au@Cu_2O-160 catalyst, rather than from simple chemical reduction by $NaBH_4$.

To evaluate the long-term stability and reusability of the Au@Cu_2O-160 catalyst, eight consecutive cycles of photocatalytic degradation of MO were performed under identical conditions. As shown in Fig. S7, the degradation efficiency remained above 90% even after eight cycles, with only a slight decrease in both the degradation rate per minute (Fig. S7A) and the overall conversion rate (Fig. S7B). This slight decrease is primarily attributed to the inevitable physical loss of catalyst particles during centrifugation due to the small reaction volume, rather than deactivation of the catalyst itself. These results demonstrate that the Au@Cu_2O-160 composite possesses excellent photocatalytic stability and reusability, which is essential for practical environmental remediation applications. Meanwhile, in order to evaluate the stability of the Au@Cu_2O-160 catalyst, the photocatalytic degradation rate constant was measured at different time intervals after synthesis. As shown in Fig. S7C, after being stored at room temperature for 3 days, 7 days and 15 days, the photocatalytic degradation rate slightly decreased. The slight decline in activity might be due to the slight surface oxidation of the Cu_2O shell when exposed to air, rather than the structural degradation of the catalyst. These results indicate that Au@Cu_2O-160 composites have excellent stability, which is crucial for practical environmental remediation applications.

Figure 5 systematically investigates the optical response and local electric field enhancement of Au nanocups and their composite structures with Cu_2O (Au@Cu_2O) using finite-difference time-domain (FDTD) simulations, corroborating the experimental findings. Figure 5A and B present the simulated extinction spectra for pure Au nanocups and the Au@Cu_2O-160 composite, respectively. The simulation results show a distinct LSPR peak for Au nanocups around 550 nm, which is in good agreement with the experimental spectrum. After coating with the Cu_2O shell, the Au resonance peak redshifts, and a broadened absorption band attributed to Cu_2O appears in the 500–600 nm range, further confirming the modulating effect of the Cu_2O shell on the optical properties of the Au nanocups, consistent with the experimental trend. Figure 5C and D further illustrate the electric field distributions of the two structures under resonance wavelength excitation. For pure Au nanocups (Fig. 5C), the electric field enhancement is mainly concentrated at the rim regions of the cup opening, forming typical "hot spot" distributions—a unique advantage of Au nanocups over conventional Au nanospheres, which is closely related to the local electromagnetic field concentration caused by their open asymmetric structure. In the Au@Cu_2O-160 structure (Fig. 5D), the electric field distribution area is significantly expanded, and the overall enhancement intensity is further increased, especially at the Au-semiconductor interface region. Further studies through FDTD simulation have shown that with the increase of Cu_2O shell thickness, when the Cu_2O shell thickness increases from Au@Cu_2O-20 (Fig. S12A) to Au@Cu_2O-80 (Fig. S12B), the electric field enhancement is gradually enhanced. The introduction of the Cu_2O shell not only alters the surrounding dielectric environment and enhances light absorption but also, due to its semiconductor properties, promotes coupling with Au, thereby forming a broader and stronger electric field enhancement zone on the composite surface. These simulation results theoretically reveal the physical mechanism behind the excellent performance of the Au@Cu_2O composite in photocatalysis: on one hand, the inherent structural features of the Au nanocups generate strong local electric fields, improving light absorption and carrier excitation efficiency; on the other hand, the introduction of the Cu_2O shell further

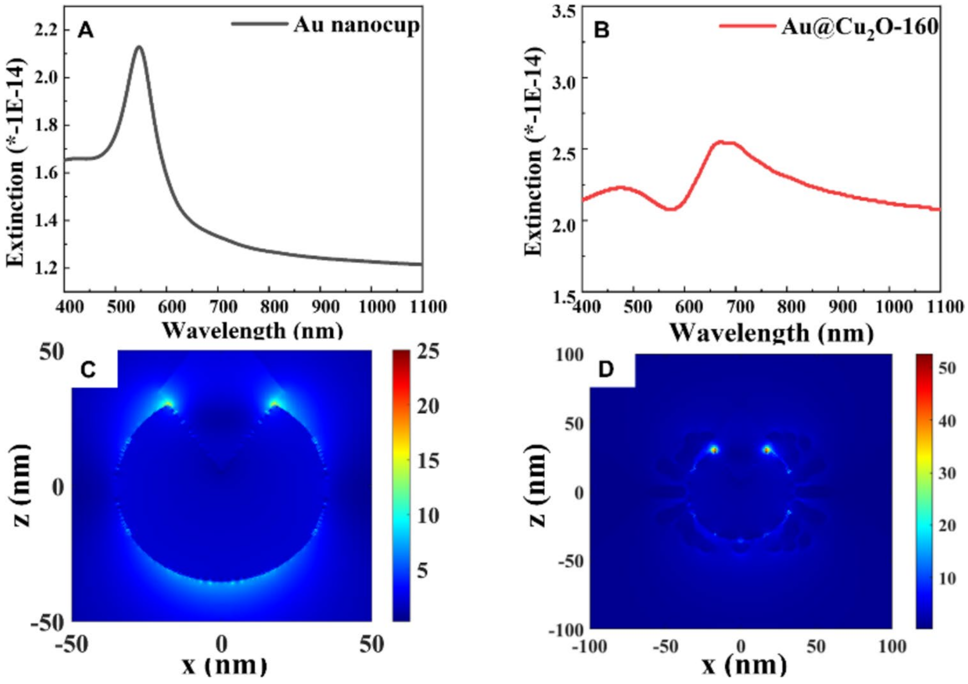

Figure 5 Finite-difference time-domain (FDTD) simulation results for various nanostructures. **A** FDTD simulation of Au nanocup. **B** FDTD simulation of Au nanocups adsorbed with Cu_2O. **C** Electric field distribution around the Au nanocup, with hot spots predominantly at the two openings of the nanocup. **D** Electric field distribution of Au nanocups coated with Cu_2O(Au@Cu_2O-160), where the incorporation of Cu_2O enhances the electromagnetic field intensity on the nanocup surface.

optimizes the electric field distribution and intensity, enhances light-matter interaction at the interface, and provides favorable electromagnetic environment support for efficient photogenerated charge separation and surface catalytic reactions. To further demonstrate the structural advantages of Au nanostructures over traditional gold forms, finite-difference time-domain simulations were conducted on AuNS@Cu_2O and AuNR@Cu_2O core–shell nanostructures with the same Cu_2O shell thickness, using Au@Cu_2O-160 as a reference. As shown in Fig. S13, the electric field distributions of the three forms vary greatly. The simulation results show that the electric field enhancement of AuNS@Cu_2O and AuNR@Cu_2O is mainly concentrated on the particle surface, and the enhancement multiple is limited. The electric field enhancement of Au nanocup@Cu_2O is mainly concentrated at the edge of the cup mouth, forming a strong "hot spot" distribution, and the maximum electric field enhancement multiple is significantly higher than the former two. These comparative simulation results provide strong quantitative evidence that specific nanocup geometers play a crucial role in achieving enhanced photocatalytic performance, surpassing the general plasma effects of Au nanostructures.

To further investigate the influence of other synthesis conditions on the structure and performance of the Au nanocup@Cu_2O composites, we systematically studied the effects of varying the amounts of $HAuCl_4$ and the PbS template volume in the growth solution on the resulting Au nanocups and their subsequent Cu_2O coating. Figure S8 shows the normalized extinction spectra of Au nanocups prepared by adjusting the $HAuCl_4$ concentration (Fig. S8A) and the PbS seed volume (Fig. S8B). The results indicate that as the amount of $HAuCl_4$ increases, the LSPR peak of the Au nanocups gradually redshifts and intensifies. Similarly, increasing the PbS template volume also leads to an LSPR peak redshift, demonstrating that the opening structure and size of the Au nanocups can be tuned via the template amount. With the $CuCl_2{\cdot}2H_2O$ addition fixed at 160 μL, we further explored the influence of PbS template volume and $HAuCl_4$ amount on the photocatalytic performance of the Au@Cu_2O-160 composites. The corresponding photocatalytic degradation curves of MO for these composites are shown in Figs. S9 (varying $HAuCl_4$ concentration) and S10 (varying PbS volume). As shown in Fig. S11, although the amounts of PbS and $HAuCl_4$ varied within a certain range, the photocatalytic degradation rates of the resulting composites did not show significant differences, all maintaining a relatively high activity level. Among them, the sample prepared with 0.2 mL $HAuCl_4$ and 0.16 mL PbS exhibited the relatively optimal catalytic rate. This phenomenon can be understood for the following reasons: First, under the condition of a fixed Cu_2O shell thickness (i.e., the same $CuCl_2$ amount), although the structural parameters of the Au core (e.g., size, opening morphology) adjust with changes in PbS and $HAuCl_4$ amounts, the coupling between its LSPR enhancement effect and the Cu_2O shell approaches saturation, and the charge separation efficiency at the formed Au-Cu_2O Schottky junction tends to stabilize, leading to no substantial fluctuation in catalytic performance. Second, the open structure of the Au nanocups inherently possesses a high specific surface area and "hot spot" density, enabling them to maintain good light harvesting and carrier injection capabilities even with fine-tuning of synthesis parameters. Finally, the ratio of 0.2 mL $HAuCl_4$ to 0.16 mL PbS might achieve the optimal match between the Au core morphology and the Cu_2O shell coverage, ensuring sufficient plasmonic resonance strength while avoiding prolonged charge recombination paths or active site shielding due to an excessively large Au core, thereby exhibiting slightly superior catalytic performance.

Figure 6 illustrates, via a schematic diagram, the microscopic process and band diagram for the photocatalytic degradation of methyl orange by the Au nanocup@Cu_2O composite under visible-light irradiation. Figure 6A depicts the band alignment and Schottky barrier formation mechanism at the Au-Cu_2O heterojunction. Cu_2O is a typical p-type semiconductor with its valence band (VB) position at approximately + 1.2 eV, conduction band (CB) at about − 1.0 eV, yielding a bandgap of ~ 2.17 eV. The Fermi level of metallic Au is around + 0.5 eV. Due to the work function difference, electrons tend to transfer from Au to Cu_2O, establishing an effective Schottky barrier that helps suppress electron back-transfer and promotes the spatial separation of photogenerated carriers. Figure 6B details the electron transfer and reaction pathways during the catalytic degradation process. Under visible-light irradiation, Cu_2O absorbs photons to generate electron-hole pairs. Driven by the electric field, electrons migrate toward Au while holes remain in the VB of Cu_2O, achieving directional separation. The LSPR effect of Au further enhances visible-light absorption and can supplement electrons into the CB

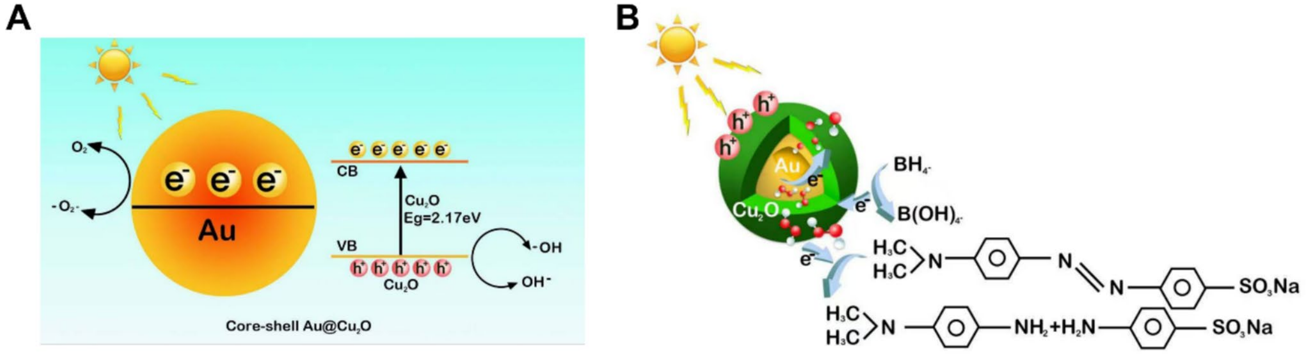

Figure 6 Schematic illustration of the Au@Cu_2O catalytic mechanism. **A** Band structure diagram of Au and Cu_2O within Au@Cu_2O and a schematic of the electron transfer process. **B** Description of the proposed theoretical mechanism for MO photocatalytic reduction facilitated by Au@Cu_2O.

of Cu_2O via a hot-electron injection mechanism. In the catalytic system, $NaBH_4$ acts as an electron donor adsorbed on the Cu_2O surface, providing electrons to the VB, thereby further increasing the concentration of reductive electrons in the system and enabling efficient MO degradation. This mechanism is further supported by the time-resolved photoluminescence (TRPL) spectra reported in the literature. Xu et al. demonstrated that the formation of the Au-Cu_2O heterojunction significantly shortened the exciton lifetime from 2.51 (Cu_2O structure) to 0.93 ns (core–shell structure), confirming the effective charge separation at the Au-Cu_2O interface [41]. This mechanism indicates that the photocatalytic enhancement of the Au cup@Cu_2O composite stems from a synergistic interplay of three factors: the heterojunction formed between Au and Cu_2O promotes efficient carrier separation; the LSPR effect of Au nanocups synergistically enhances light absorption and hot-electron injection and $NaBH_4$, as an external electron donor, boosts the reducing capability. Together, these factors construct an efficient electron-transfer platform, significantly improving the catalytic performance of the composite under visible light and providing theoretical support for designing plasmonic-semiconductor catalytic systems with directional electron transfer pathways.

Conclusions

In summary, we have successfully synthesized Au nanocup@Cu_2O nanoparticles using Au nanocups with an open structure as the core and a low-temperature surfactant-assisted method, achieving a well-defined Cu_2O coating. By varying the volume of added $CuCl_2$ precursor, control over the Cu_2O shell thickness on the Au nanocups was accomplished, enabling size-tunable Au@Cu_2O structures. Analysis of the results revealed that the synthesized Au nanocup@Cu_2O nanoparticles exhibit a distinct LSPR response, the intensity of which is closely related to the Cu_2O shell thickness. Furthermore, their excellent photocatalytic activity was verified through the $NaBH_4$-assisted reduction of methyl orange under light irradiation. The photocatalytic rate increased significantly with increasing $CuCl_2$ volume, indicating that the synergistic effect strengthens as the Cu_2O shell thickness grows. Compared to individual Au nanocups and Cu_2O particles, the Au nanocup@Cu_2O composites demonstrate a remarkable advantage in promoting the reaction rate. This enhancement is primarily attributed to the LSPR effect of the Au nanocups, which efficiently absorbs visible light and generates high-energy hot electrons. These hot electrons are injected into the conduction band of Cu_2O, leading to highly efficient photogenerated carrier separation. Simultaneously, a Schottky barrier forms at the Au-Cu_2O interface, preventing electrons from back-transferring from Cu_2O to Au. This significantly prolongs the lifetime of photogenerated carriers, improves quantum efficiency, and suppresses electron-hole recombination. Based on the findings, this work confirms the advantages of Au nanocup@Cu_2O nanostructures in plasmon-mediated photocatalytic reactions, highlights their application prospects in photocatalysis, and lays a foundation for the development of other plasmon-regulated photocatalytic materials.

Experimental

Chemicals

Cetyltrimethylammonium bromide (CTAB, 99%) was purchased from TCI America. Ascorbic acid (AA, 99.99%), hydrogen tetrachloroaurate(III) ($HAuCl_4$), hydrochloric acid (HCl, 37 wt.% in water), copper(II) chloride dihydrate ($CuCl_2·2H_2O$, 99.99%), sodium dodecyl sulfate (SDS, 92.5%), hydroxylamine hydrochloride ($NH_2OH·HCl$, 99.99%), and methyl orange (MO, 96%) were obtained from Shanghai Macklin Biochemical Co., Ltd. Sodium borohydride ($NaBH_4$, 98%) was purchased from Shanghai Aladdin Biochemical Technology Co., Ltd. Sodium hydroxide (NaOH, 96.0%) and ethanol (EtOH, 99.7%) were supplied by Hangzhou Highfine Chemical Co., Ltd. Ultrapure water (Millipore Milli-Q grade) with a resistivity of 18.2 MΩ cm was used throughout. All chemicals were used as received without further purification.

Synthesis of PbS octahedra

PbS nano-octahedra were synthesized by mixing 2.04 mL of thioacetamide (TAA, 0.5 M), 2.57 mL of cetyltrimethylammonium bromide (CTAB, 0.1 M), 2.04 mL of lead acetate ($Pb(Ac)_2$, 0.5 M), and 4.10 mL of acetic acid (HAc, 1 M), and then injecting the mixture into 34.26 mL of deionized water. After thorough mixing, the solution was placed in an oven at 90 °C for 8 h. After heating, the solution was taken out and cooled for subsequent use.

Synthesis of Au nanocup

Au nanocups were synthesized using a reported template-etching method [20, 21]. Specifically, 0.2 mL of 10 mM $HAuCl_4$ and 0.2 mL of 0.1 M ascorbic acid were sequentially added to 10 mL of 0.05 M CTAB solution. After mixing, 0.16 mL of the as-prepared PbS nano-octahedra solution was added. The mixture was left standing at room temperature for 2 h. Subsequently, 0.2 mL of 5 M HCl was added, and the solution was heated at 60 °C for 12 h to completely etch the PbS template. The resulting product was centrifuged at 8000 rpm for 6 min, washed with water, and redispersed to obtain the Au nanocup colloidal solution.

Synthesis of Au@Cu_2O composites

Different volumes of $CuCl_2·2H_2O$ (0.1 M) were added to sodium dodecyl sulfate (SDS, 0.23 M, 0.75 mL). Subsequently, 4 mL of the as-prepared Au nanocup solution was added. The mixture was stirred on a magnetic stirrer at 600 rpm for 1 min, then cooled in an ice-water bath at 4 °C for 5 min. Sodium hydroxide (0.125 mL, 1 M) and hydroxylamine hydrochloride (0.35 mL, 0.1 M) were then added. The resulting solution was kept static in the 4 °C ice-water bath for 1 h. After standing, the product was centrifuged at 8000 rpm for 5 min and stored in ethanol. Pure Cu_2O nanoparticles were synthesized following the same procedure, except the Au nanocup precursor was replaced with deionized water, while all other conditions remained unchanged. The synthesized Cu_2O particles were also centrifuged and stored in ethanol. It should be noted that the Cu^{2+} concentration was kept consistent during the synthesis of pure Cu_2O and the Au@Cu_2O composite particles for fair performance comparison.

Characterization

Optical extinction spectra were recorded using a Shimadzu UV-1900i spectrophotometer with a 10 mm optical path length. Scanning electron microscopy (SEM) images were acquired on a ZEISS Sigma 360 field-emission SEM. Transmission electron microscopy (TEM) images were acquired using a Hitachi HT7800 operated at an acceleration voltage of 100 kV. Particle sizes were measured from SEM images using ImageJ software. Elemental analysis was performed using energy-dispersive X-ray spectroscopy (EDS). X-ray photoelectron spectroscopy (XPS) data were obtained on a Thermo Scientific K-Alpha spectrometer. X-ray diffraction (XRD) data were obtained on a Panalytical Empyrean instrument.

Photocatalytic degradation of methyl orange

In the photocatalytic degradation experiment of methyl orange, the prepared catalytic nanoparticles (Au@Cu_2O-20/40/80/160, Au nanocups, and Cu_2O nanoparticles) were collected by centrifugation and uniformly dispersed in Milli-Q water via sonication. In a cuvette, 1 mL of 0.15 mM MO solution and 50 μL of freshly prepared 0.1 M $NaBH_4$ solution were mixed, followed by the addition of 20 µL of the nanocatalyst dispersion. The catalytic reaction was conducted under irradiation from a 250 W xenon lamp (HDL-II, Suzhou Bataijia Optoelectronics Technology Co., Ltd., China). The absorption peak of MO at 462 nm was monitored using a UV–Vis–NIR spectrophotometer (UV-1900i, Shimadzu). Absorption spectra were recorded at 1-minute intervals until the peak at 462 nm almost completely disappeared and the color changed from orange to transparent. Each experiment was repeated five times to ensure data reliability and minimize experimental error.

FDTD simulations

Finite-difference time-domain (FDTD) simulations were performed using FDTD Solutions software (Lumerical Solutions, Inc.) to simulate the extinction spectra of the Au@Cu_2O nanostructures. The refractive index of the surrounding medium was set to 1.33 (water) for Au nanocups and 1.361 (anhydrous ethanol) for Au nanocup@Cu_2O. Perfectly matched layer (PML) boundary conditions were applied. The mesh size was set to 0.5 nm for the Au nanocup region and 1 nm for the Au nanocup@Cu_2O region. The light source was a plane wave covering wavelengths from 400 to 1100 nm. The Au core was modeled as a sphere with an opening, and the Cu_2O shell was modeled with varying numbers of Cu_2O particles to represent different shell thicknesses. For comparison, a Au@Cu_2O with Au nanospheres and Au nanorods as the core was also simulated, in which the shell thickness and the size of the Au nanocore were close to those of the gold cup. Dielectric function data for Au and Cu_2O were taken from Palik [42].

Acknowledgements

The authors thank Sudan Shen for her assistance in TEM at State Key Laboratory of Chemical Engineering (Zhejiang University). T.S.D. acknowledges financial support from Zhejiang Provincial Natural Science Foundation (Grant: LY24F050008) and National Natural Science Foundation of China (NSFC, Grant: 61905056). This work was also supported in part by Shanghai Industrial Collaborative Innovation Project under grant HCXBCY-2024-051.

Data availability

The data that support the findings of this study are available from the corresponding author upon reasonable request.

Declarations

Conflict of interest The authors declare no conflict of interest.

Supplementary Information The online version contains supplementary material available at https://doi.org/10.1007/s10853-026-13004-3.

References

[1] Sahu K, Bisht A, Dutta A et al (2021) Morphological, optical, catalytic and photocatalytic properties of RF magnetron sputtered Au-Cu_2O-CuO nanocomposite thin films. Surf Interfaces 26:101436

[2] Huang Y, Chen C, Tan H et al (2024) A stimulus-responsive ternary heterojunction boosting oxidative stress, cuproptosis for melanoma therapy. Small 20:2401147

[3] Yuan X, Pei F, Luo X et al (2021) Fabrication of ZnO/Au@Cu_2O heterojunction towards deeply oxidative photodegradation of organic dyes. Sep Purif Technol 262:118301

[4] Mindil A, Mohamed SH, Alsubaie AS, Rabia M (2024) WO_3/Cu_2O-CuO and WO_3/Au/Cu_2O-CuO heterojunctions photocatalysts for self-cleaning and photocatalytic degradation of organic pollutants applications. Phys Scr 99:105964

[5] Okoye PC, Azi SO, Qahtan TF et al (2023) Synthesis, properties, and applications of doped and undoped CuO and Cu_2O nanomaterials. Mater Today Chem 30:101513

[6] Chen X, Cui K, Hai Z et al (2021) Hydrothermal synthesis of Cu_2O with morphology evolution and its effect on visible-light photocatalysis. Mater Lett 297:129921

[7] Jiang D, Zhang Y, Li X (2019) Synergistic effects of CuO and Au nanodomains on Cu_2O cubes for improving photocatalytic activity and stability. Chin J Catal 40:105–113

[8] Wu S-C, Tan C-S, Huang MH (2017) Strong facet effects on interfacial charge transfer revealed through the examination of photocatalytic activities of various Cu_2O-ZnO heterostructures. Adv Funct Mater 27:1604635

[9] Zhou M, Li C, Fang J (2021) Noble-metal based random alloy and intermetallic nanocrystals: syntheses and applications. Chem Rev 121:736–795

[10] Ha M, Kim J-H, You M et al (2019) Multicomponent plasmonic nanoparticles: from heterostructured nanoparticles to colloidal composite nanostructures. Chem Rev 119:12208–12278

[11] Wang L, Ge J, Wang A et al (2014) Designing *p*-type semiconductor-metal hybrid structures for improved photocatalysis. Angew Chem Int Ed 53:5107–5111

[12] Xie C, Niu Z, Kim D et al (2020) Surface and interface control in nanoparticle catalysis. Chem Rev 120:1184–1249

[13] Shen B, Xia Y, Zhou Y et al (2025) Synthesis of highly-ordered ternary CeO_2-AuNR-Cu_2O Janus structure with dual Schottky junctions for highly efficient photocatalysis. Sci China Mater 68:1906–1917

[14] Kumar A, Singh H, Sahay S, Balasubramanian KB (2022) Charge injection into electrodeposited Cu_2O from metallic stacks and graphene. IEEE Trans Electron Devices 69:5755–5759

[15] Hu Z-J, Mi Y et al (2019) Multiplasmon modes for enhancing the photocatalytic activity of Au/Ag/Cu_2O core-shell nanorods. Nanoscale 11:16445–16454

[16] Wi DH, Yang H, Kim Y et al (2023) Metal-semiconductor-metal ternary heteronanocrystals with multiple plasmonic effects for efficient photocatalysis. J Mater Chem A 11:1343–1350

[17] Wang J, Ji H, Zhang B et al (2025) Tailoring shell thickness in Au@Cu_2O nanoparticles for enhanced mimetic peroxidase activity: a colorimetric aptasensor for zearalenone detection. Microchim Aata 192:339

[18] Xu W, Zhang L, Cang L et al (2025) Modulation of highly ordered Au-Cu_2O core-satellite nanostructures for enhanced photocatalytic performance. Inorg Chem 64:19430–19441

[19] Jiang R, Qin F, Liu Y et al (2016) Gold nanocups: colloidal gold nanocups with orientation-dependent plasmonic properties (Adv. Mater. 30/2016). Adv Mater 28:6266–6266

[20] Gao A, Xu W, Ponce de León Y et al (2017) Nanostructures: controllable fabrication of Au nanocups by confined-space thermal dewetting for OCT imaging (Adv Mater 26/2017). Adv Mater 29:1701070

[21] Zhang H, Lam SH, Guo Y et al (2021) Selective deposition of catalytic metals on plasmonic Au nanocups for room-light-active photooxidation of o-phenylenediamine. ACS Appl Mater Interfaces 13:51855–51866

[22] Zhang F, Yan H, Li G et al (2024) Photothermal conversion property of (Au nanocup)–(Cu_2O nanocube) hybrids supported by MXene nanosheets. Cryst Growth Des 25:367–375

[23] Ding S-J, Zhang H, Yang D-J et al (2019) Magnetic plasmon-enhanced second-harmonic generation on colloidal gold nanocups. Nano Lett 19:2005–2011

[24] Zhao Y-X, Zheng Z-X, Zhang L-S et al (2023) Optimized electromagnetic enhancement and charge transfer in MXene/Au/Cu_2O hybrids for achieving efficient SERS. Phys Chem Chem Phys 25:15209–15218

[25] Dou Y-Q, Deng T-S, Zhang Q et al (2023) A study of size-controlled Au@Cu_2O nanocomposite for highly improved methyl orange catalytic performances. J Mater Sci 58:7583–7593

[26] Yang G, Tao Y, Cheng Q et al (2025) Shell dependence of highly tunable circular dichroism in chiral hybrid plasmonic nanomaterials for chiroptical applications. ACS Nano 19:2961–2974

[27] Wu J-Y, Lai T-H, Fang M-J et al (2022) Electronic interactions and charge-transfer dynamics for a series of yolk-shell nanocrystals: implications for photocatalysis. ACS Appl Nano Mater 5:8404–8416

[28] Lai T-H, Tsao C-W, Fang M-J et al (2022) Au@Cu_2O core-shell and Au@Cu_2Se yolk-shell nanocrystals as promising photocatalysts in photoelectrochemical water splitting and photocatalytic hydrogen production. ACS Appl Mater Interfaces 14:40771–40783

[29] Cao C, Xu W, Chen D et al (2026) NIR-II photocatalytic-triggered pyroptosis via built-in electric field-enhanced reactive oxygen species generation in Au-Cu_2O nanodumbbells. ACS Nano 20:1386–1398

[30] Jia H, Li F, Chow TH et al (2022) Construction of spatially separated gold nanocrystal/cuprous oxide architecture for plasmon-driven CO_2 reduction. Nano Lett 22:7268–7274

[31] Yang Y, Zhang B, Sun X et al (2025) Tuning the modal coupling in three-dimensional Au@Cu_2O@Au core-shell-satellite nanostructures for enhanced plasmonic photocatalysis. Chem Sci 16:8069–8081

[32] Zhang H, Gao H, Yang W et al (2025) Enantioselective photocatalytic discrimination of D-and L-dihydroxyphenylalanine (Dopa) by chiral Au@Cu_2O-Cu2S nanoparticles. J Alloys Compd 1042:184042

[33] Sayed M, Yu J, Liu G, Jaroniec M (2022) Non-noble plasmonic metal-based photocatalysts. Chem Rev 122:10484–10537

[34] Ahn Y, Park J, Park M et al (2022) Combinatorial selective synthesis and excitation experiments for quantitative analysis of effects of Au on a semiconductor photocatalyst. Chem 8:2485–2497

[35] Huang Q, Yang J, Qi F et al (2022) Visible light driven photocatalytic reduction of CO_2 on Au-Pt/Cu_2O/ReS_2 with high efficiency and controllable selectivity. Chem Eng J 437:135299

[36] Zhu Q, Wang Y, Chen F et al (2023) Enhanced photocatalytic H_2 production performance of Au@Cu_2O-Ta_3N_5 discrete ternary core-shell spheres. Appl Surf Sci 635:157682

[37] Li Y, Yan H, Zhou R et al (2025) Trace detection of deltamethrin via Au/Cu_2O/ZnO SERS substrates with multiple heterojunctions. Langmuir 41:3822–3831

[38] Wei M-Z, Deng T-S, Zhang Q et al (2021) Seed-mediated synthesis of gold nanorods at low concentrations of CTAB. ACS Omega 6:9188–9195

[39] Zhang Z, Guo H, Li S, Gao S, Wang X, Li M, Yan W, Xu H (2025) Cavity-confined Au@Cu_2O yolk-shell nanoreactors enable switchable CH_4/C_2H_4 selectivity. Nat Commun 16:7559

[40] Galindo C, Jacques P, Kalt A (2000) Photodegradation of the aminoazobenzene acid orange 52 by three advanced oxidation processes: UV/H_2O_2, UV/TiO_2 and VIS/TiO_2. J Photochem Photobiol A Chem 130:35–47

[41] Xu W, Xiao R, An S et al (2023) Engineering the Au-Cu2O crystalline interfaces for structural and catalytic integration. Small 19:2300587

[42] Palik ED, Ghosh G (1998) Handbook of optical constants of solids. Academic Press, San Diego